Lattice Boltzmann numerical simulation and experimental research of dynamic flow in an expansion-contraction microchannel

Di Jiang, Dongke Sun, Nan Xiang, Ke Chen, Hong Yi, and Zhonghua Ni[a)]
Jiangsu Key Laboratory for Design and Manufacture of Micro-Nano Biomedical Instruments, School of Mechanical Engineering, Southeast University, Nanjing 211189, China

(Received 16 April 2013; accepted 14 June 2013; published online 26 June 2013)

This paper applies the lattice Boltzmann method (LBM) to a 3D simulation of micro flows in an expansion-contraction microchannel. We investigate the flow field under various inlet flow rates and cavity structures, and then systematically study the flow features of the vortex and Dean flow in this channel. Vortex formation analysis demonstrates that there is no observable vortex generated when the inlet flow rate is low enough. As the inlet flow rate increases, a small vortex first appears near the inlet, and then this vortex region will keep expanding until it fully occupies the cavity. A smaller cavity width may result in a larger vortex but the vortex is less influenced by cavity length. The Dean flow features at the outlet become more apparent with increasing inlet flow rate and more recirculation regions can be observed in the cross-section under over high inlet flow rate. In order to support the simulation results, some experimental processes are conducted successfully. It validates that the applied model can accurately characterize the flow in the microchannel. Results of simulations and experiments in this paper provide insights into the design and operation of microfluidic systems for particle/cell manipulation.
 [http://dx.doi.org/10.1063/1.4812456]

I. INTRODUCTION

Microfluidics provides an important approach for the pretreatment,[1] manipulation,[2] and detection[3] of bio-macromolecules or cells due to its distinct advantages such as portability, rapidity, low cost, and small volume consumption.[4–7] In a microfluidic system, flow features, which in a large part determine the manipulation functions of the system,[8–11] can be obtained by regulating the structure of the microchannels. The microvortex, a special fluid effect generated in sudden expansion or curved microchannels, is of great importance for particle manipulation. Therefore, studies on this specific hydrodynamic effect have attracted significant attention.

Researchers have been particularly interested in the theoretical analysis and experimental investigation on the formation of vortices and Dean flows in different microchannel configurations. For example, Bălan *et al.*[12] investigated the dynamics of the vortices generated in the vicinity of Y- and T-microbifurcations with one occluded branch. The velocity distribution and streamlines were obtained through the experiments and commercial software FLUENT. Tsai *et al.*[13–15] focused on the formation of recirculation zones in a sudden expansion microchannel. They found that Reynolds number and aspect ratio are both influential factors for flow patterns in microchannels. Yu *et al.*[16] studied the gas and liquid flows in microchannels with small cavities by utilizing CFD-ACE+ solver. In their research, control parameters for flow separation occurrence in a cavity were presented. Park *et al.*[17] studied the flow pattern in an axisymmetric multi-orifice microchannel with particle-focusing function, and the streamlines of the vortices in the expansion region was simulated using the COMSOL Multiphysics solver. Furthermore,

[a)]Author to whom correspondence should be addressed. Electronic mail: nzh2003@seu.edu.cn.

some applications of the microvortices in an expansion-contraction microchannel, such as cell trapping and cell labeling,[18,19] have been presented in recent years. According to their researches, in the contraction part, particles flow under the balance of shear-gradient lift force and wall effect lift force. When the particles move into the expansion part, wall effect lift force disappears and the shear-gradient lift force leads particles to the vortex formed in the cavity. Since the lateral migration velocity is dependent on the particle size,[19] only particles larger than critical size can migrate into the vortex region and circle in the cavity. Besides the vortex, Dean flow in this kind of microchannel is also a promising approach for particle separation. Lee's group[20,21] demonstrated a blood plasma separation scheme by employing the unilateral contraction-expansion array microchannel with a low aspect ratio. Small particles are driven predominantly by Dean drag force while the larger ones are lifted by the inertial force and stay close to their previous positions, leading to the isolation of different size particles. The inlet flow rate should be appropriately controlled to avoid particle migration into the vortex in the cavity under an over high flow rate. However, in their reported research, the velocity distribution of the Dean flow in contraction region was simply given at a certain total flow rate.

Most of aforementioned hydrodynamics simulation works were performed by utilizing commercial softwares which are based on conventional computational fluid dynamic (CFD), and in their simulations the vortex development and the Dean flow formation have not been elaborated clearly. In this research, we intend to apply the lattice Boltzmann method (LBM) to systematically study the vortices and Dean flows in the expansion-contraction microchannel. This alternative method is not only powerful in simulating the flow field under complex boundary conditions[22] but also more flexible for users to adjust the algorithm to the practical problems. For the same accuracy of the simulation, traditional macroscopic momentum balance methods used in CFD require much more memory than the LBM to generate a satisfactory body-fitted grid,[23] and this is because LBM is based on a different concept, mesoscopic kinetic theory.

In this work, vortices and Dean flows in the expansion-contraction microchannel are systematically studied with LBM. With increasing inlet flow rate and varying cavity dimensions, the simulations of the flow fields will constitute a complete picture of vortices and Dean flows development. To support the consequence obtained from the simulation, several experimental processes are conducted carefully. A corresponding microfluidic device is fabricated and the flow field is observed under the microscope with the vortex clearly recorded. The experimental results are well agreed with those obtained from computational simulation, which illustrates that the LBM used in this work can accurately describe the flow dynamics in this expansion-contraction microchannel. The detailed results demonstrated in this work provide better insights into the design and operation of high-throughput particle/cell manipulation.

II. MATHEMATICAL DESCRIPTION

A. Single-relaxation-time D3Q19 model

The flow field is described by incompressible Navier-Stokes equations which are solved by the lattice Bhatnagar–Gross–Krook 3-dimensional 19-bit (LBGK-D3Q19) model. The corresponding discrete lattice Boltzmann equation[24] can be expressed as

$$f_i(\boldsymbol{x}+\boldsymbol{c}_i\Delta t, t+\Delta t) = f_i(\boldsymbol{x},t) + \frac{1}{\tau}[f_i^{eq}(\rho,\boldsymbol{u}) - f_i(\boldsymbol{x},t)], \quad (i=0,1,2,...,18), \tag{1}$$

where $f_i(\boldsymbol{x},t)$ is the distribution function at position $\boldsymbol{x}$ and time t associated with the discrete velocity $\boldsymbol{c}_i$ defined as $c=\Delta x/\Delta t$, Δx and Δt are the lattice grid spacing and the time step; τ is the nondimensional relaxation time and f_i^{eq} is the equilibrium distribution function

$$f_i^{eq} = w_i\rho\left[1+\frac{\boldsymbol{c}_i\cdot\boldsymbol{u}}{c_s^2}+\frac{(\boldsymbol{c}_i\cdot\boldsymbol{u})^2}{2c_s^4}-\frac{u^2}{2c_s^2}\right]. \tag{2}$$

This equation is a spatial discrete form of Maxwell-Boltzmann distribution.

The 19 discrete velocities in the D3Q19 model can be given by

$$\boldsymbol{c} = c\begin{bmatrix} 0 & 1 & -1 & 0 & 0 & 0 & 0 & 1 & -1 & 1 & -1 & 1 & -1 & -1 & 1 & 0 & 0 & 0 & 0 \\ 0 & 0 & 0 & 1 & -1 & 0 & 0 & 1 & -1 & -1 & 1 & 0 & 0 & 0 & 0 & 1 & -1 & 1 & -1 \\ 0 & 0 & 0 & 0 & 0 & 1 & -1 & 0 & 0 & 0 & 0 & 1 & -1 & 1 & -1 & 1 & -1 & -1 & 1 \end{bmatrix}, \tag{3}$$

sound speed of the model $c_s = \frac{c}{\sqrt{3}}$ and weight coefficients

$$w_i = \begin{cases} \frac{1}{3}, & i = 0 \\ \frac{1}{18}, & i = 1, 2, 3, ..., 6 \\ \frac{1}{36}, & i = 7, 8, 9, ..., 18. \end{cases}$$

The fluid density ρ and velocity $\boldsymbol{u}$ can be calculated by

$$\rho = \sum_i f_i, \quad \rho \boldsymbol{u} = \sum_i \boldsymbol{c}_i f_i. \tag{4}$$

The relation between kinematic viscosity ν and the nondimensional relaxation time τ is

$$\nu = \frac{1}{3}\frac{\Delta x^2}{\Delta t}\left(\tau - \frac{1}{2}\right). \tag{5}$$

B. Boundary conditions employed

The halfway bounce-back scheme,[25] which locates the wall at the halfway between a flow node and the adjacent solid node, is employed in this simulation. The solid node neighboring a flow node is marked as a bounce-back node. When the distribution function f flows to a bounce-back node, it will flow back immediately and then the next step begins. The flow is driven by the non-equilibrium extrapolation method of Guo *et al.*,[26] which is applied here for inlet and outlet pressure boundary conditions.

C. Model validation

In order to validate the present numerical model, simulation of a lid-driven flow in a cubic cavity ($1 \times 1 \times 1$) is performed here. The configuration of the cavity is shown in Figure S1(a) of the supplementary material.[27] The top wall moves along the x direction with a constant velocity $u_x = 0.1$ while other walls are fixed. The mesh of the computational domain is uniform and of size $101 \times 101 \times 101$. Reynolds number ($\mathrm{Re} = UL/\nu$, U is the mean velocity, and L is the characteristic linear dimension) is chosen as 1000, resulting in $\nu = 0.01$ and $\tau = 0.53$. From Figures S1(b) and S1(c) of the supplementary material,[27] it is found that the present solution is in good agreement with the results of Du *et al.*[28] and Guj *et al.*,[29] which conforms the validity of the numerical model employed in this paper.

III. RESULTS AND DISCUSSION

A. Problem description

The schematic view of the expansion-contraction microchannel is shown in Figure 1. The channel widths of contraction and expansion regions are 50 μm and 350 μm, respectively. By using a uniform mesh with the lattice grid spacing set as $\Delta x = 2 \times 10^{-6}$ m and defining the

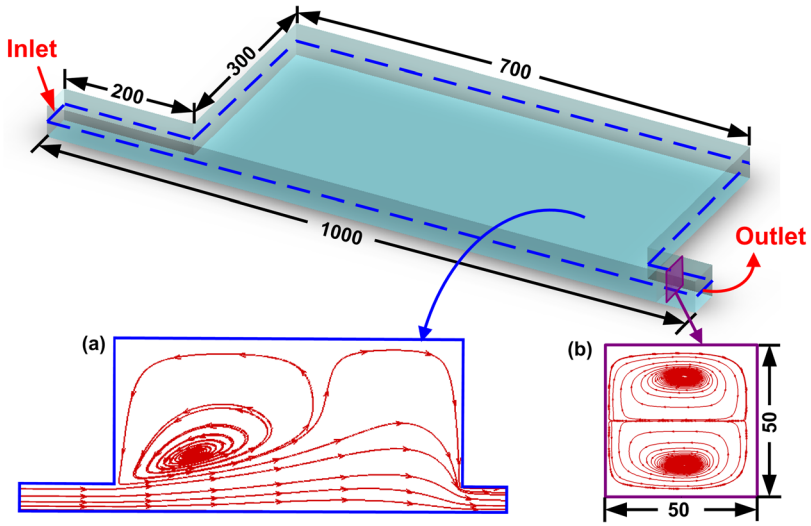

FIG. 1. Schematic view of the microchannel (unit: μm). (a) Median horizontal plane and (b) cross-section at the outlet of the microchannel.

kinematic viscosity as $\nu = 1.0855 \times 10^{-6}$ m^2/s, the relation between Δt and τ can be obtained through Eq. (5). According to the definition of Reynolds number Re, a wide range of Re is obtained here by changing the volumetric flow rate. In the simulation, nondimensional mean inlet velocity is always set at 0.04 under different flow rates, so that Mach number Ma (Ma = U/c) in LBM can satisfy the requirement $Ma \ll 1$. Time step Δt and nondimensional relaxation time τ vary with Re. Detailed parameters are demonstrated in Table I.

B. Vortex formation in an expansion-contraction microchannel

The features of the vortex in the cavity of the expansion-contraction microchannel are greatly determined by the Reynolds number and cavity structure. First, we perform the simulation of the flow field under seven different inlet flow rates with the LBM code. The velocity distribution and streamlines obtained from the simulation are shown in Figure 2.

This figure illustrates the flow patterns in the median horizontal plane. Initially, the flow rate is set at a minimum of 50 μl/min, and there is no obvious vortex generated in the rectangular cavity. However, a small vortex begins to appear near the inlet of the cavity when the inlet flow rate is 150 μl/min. As the flow rate further increases to 250 μl/min, and then 350 μl/min, the vortex gradually moves towards the outlet with its area expanding. Finally, the vortex will occupy almost the whole expansion region of the microchannel when the flow rate is over 450 μl/min. On these occasions, the vortex acts on the main flow like a channel wall, and the main flow passes through the cavity fast with a smaller expansion.

TABLE I. Parameters selection under different volumetric flow rates.

Volumetric flow rate (μl/min)	Flow rate (m/s)	Flow rate (nondimensional)	Time step Δt (10^{-6}s)	Relaxation time τ (nondimensional)	Reynolds number
50	0.3333	0.04	0.2400	0.6954	15
150	1.0000	0.04	0.0800	0.5651	46
250	1.6667	0.04	0.0480	0.5391	77
350	2.3333	0.04	0.0343	0.5279	107
450	3.0000	0.04	0.0267	0.5217	138
550	3.6667	0.04	0.0218	0.5178	168
650	4.3333	0.04	0.0185	0.5150	199

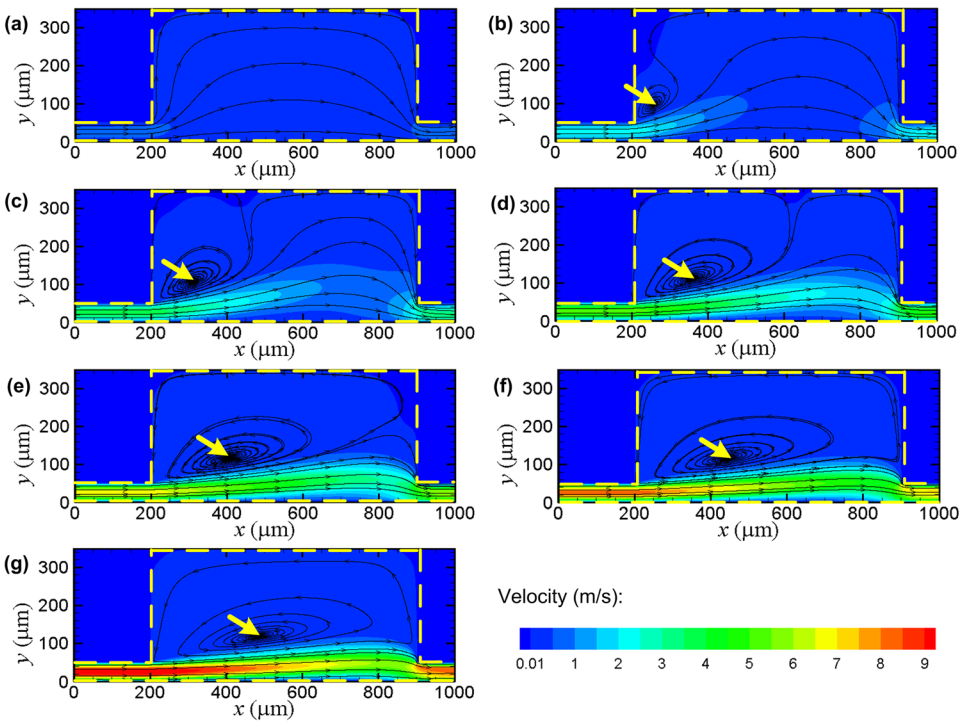

FIG. 2. Velocity (contour legend) and streamlines under various flow rates (yellow arrows point to the vortex centers): (a) 50 μl/min; (b) 150 μl/min; (c) 250 μl/min; (d) 350 μl/min; (e) 450 μl/min; (f) 550 μl/min; and (g) 650 μl/min.

To further investigate the details of the flow field in the cavity, the evolution of the vortex center under different flow rates and the x-velocity distributions through the vortex centers are described in Figure 3.

The vortex center is near the inlet of the rectangular cavity when the flow rate is slow. With a constant increment of the inlet flow rate, the vortex center moves towards the outlet at a

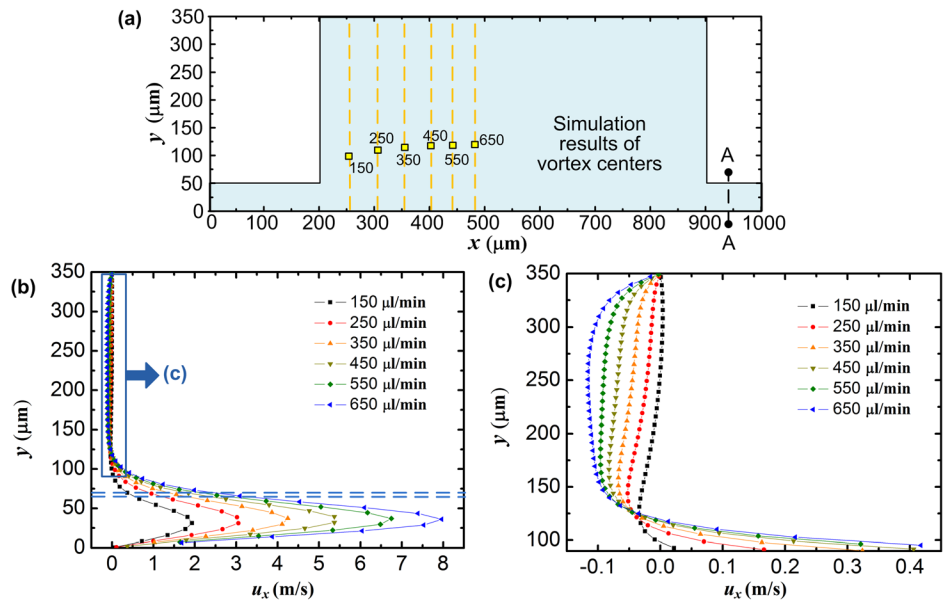

FIG. 3. Evolution of the vortex center and x-velocity distributions under different flow rates. (a) Vortex centers under different flow rates (unit: μl/min). (b) x-velocity distribution along orange dash lines passing through each vortex center in (a), and the boundaries between the vortex and main flow in each curve are located between the blue dash lines. (c) x-velocity distribution extracted from the blue box in (b).

continuously slower pace. Compared with the main flow, the flow in the vortex region has lower velocity. However, the vortex flow close to the main flow keeps a similar flow rate with the main flow in Figure 3(b), which can be explained that the vortex flow is largely driven by the main flow with fluid viscosity.[16] The *x*-velocity distribution of vortex in Figure 3(b) is extracted in Figure 3(c), which shows that the vortex also becomes stronger with the increasing inlet flow rate. Even though the *x*-velocity increment of the vortex upper region is very limited compared with the main flow, it is still notable due to the small scale of the channel. If any particles migrate into the vortex, they will be circling in the cavity with a fast-slow-fast velocity and the larger particles will occupy the inner orbits because they can provide enough inertial force to balance the consequential centrifugal force there. This particle performance has been confirmed by the research of Mach *et al.*[18] The lower pressure caused by the fluid motion narrows the vortex orbits close to the main flow and may lead redundant particles to flee from the vortex; therefore, the number of particles expected to be trapped should not exceed the capacity of the vortex.

Considering the results above, size and center position of the vortex region both vary depending on the Reynolds number. At the minimum flow rate (50 μl/min), fluid flows through the cavity with no vortices generated. As flow rate increases (150 μl/min, 250 μl/min, and 350 μl/min), a separation from the main flow is generated due to the inertial effect. Vortices are induced as the results of the flow coming back. However, when the flow rate is high enough (450 μl/min, 550 μl/min, and 650 μl/min), the flow may directly reach the cavity wall close to the outlet and then bounce back with a large region vortex forming. This large vortex can fully occupy the cavity and form a relatively closed domain which is able to trap target particles or cells by their sizes.[18,19] Through the inlet flow rate adjustment, the vortex can be generated or dismissed to store or release the particles. Since an effective vortex usually should be large enough to fully interact with the particles and store enough quantity of them, relatively higher inlet flow rate is helpful for the channel operation.

Cavity structure is another factor influencing the features of the vortex. Several flow fields with different cavity dimensions are investigated in Figure 4 and the inlet flow rate is fixed as 150 μl/min in all simulations. As we can see from the results, the reduction of the cavity width increases the ratio of the vortex region in the cavity. When the cavity is wide (700 μm, 600 μm, 500 μm), vortex region is stable but it broadens quickly as the width keeps shrinking (400 μm, 300 μm). Finally, the vortex fully occupies the cavity with a 200 μm wide opening. Comparing Figure 4(e) with Figures 4(g) and 4(h), we find that cavity length has less influence on the flow pattern here. The negative correlation between cavity width and vortex size could be employed in the new channel system design. To trap the extremely large particles (above 30 μm diameter) exclusively, Re needs to be relatively lower, thus the vortex may not be large enough. Reducing the cavity width could be a feasible structural design in this situation.

C. Dean flow in an expansion-contraction microchannel

Another important phenomenon in this expansion-contraction microchannel is Dean flow, which forms at the outlet of the microchannel. Figure 5 depicts the velocity distribution of the Dean flow in the cross-section (see A-A in Figure 3(a)) at the outlet. When the flow rate is 50 μl/min, 150 μl/min, 250 μl/min or 350 μl/min, the peak velocity in the cross-section is close to the left side wall in the figure. The reason of this phenomenon is that the flow restricted by the vortex and the cavity walls will run towards left under inertial force. In the outlet channel, median plane flow runs towards left and the flow reaching the left wall will bounce back, therefore a pair of annular velocity distributions forms in the cross-section. However, the peak velocity can return back to the center of the outlet after a short distance. As the flow rate increases to 450 μl/min, 550 μl/min, and 650 μl/min, the vortex fully occupies the cavity. In these situations, the main flow is just blocked by a corner of the cavity, and the expansion of the main flow is much smaller. For this reason, the velocity is redistributed and the peak velocity position moves from left region to the right in the cross-section. Figures 5 and 6 present that when the flow rate is 50 μl/min, the Dean flow is not very obvious. With the flow rate

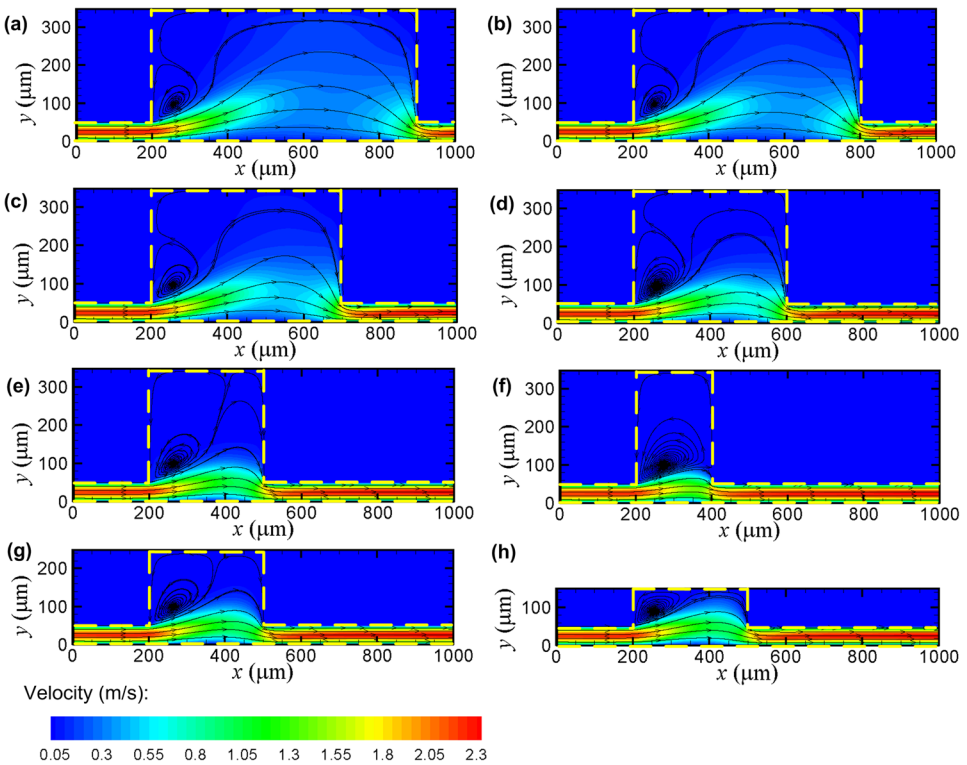

FIG. 4. Evolution of flow field in cavities with different dimensions: (a)–(f) cavities with 700-200 μm widths and 300 μm length; (g) and (h) cavities with 300 μm width and 200–100 μm lengths. The inlet flow rate is 150 μl/min in these simulations.

getting higher, the Dean flow is clearer and the annular flow in the cross-section is stretched more severely. This Dean flow effect at this flow intensity can be a very promising approach for the particle separation based on their sizes.[20,21] As the flow rate increases to 450 μl/min, the flow pattern begins to change. More recirculation regions are generated and then become stronger in the cross-section when the flow rate increases to 550 μl/min and 650 μl/min. Flow environment here is much more complex for particle transportation control. Therefore, the Re here for a particle separation channel needs to keep relatively lower to avoid the Dean flow distortion and the

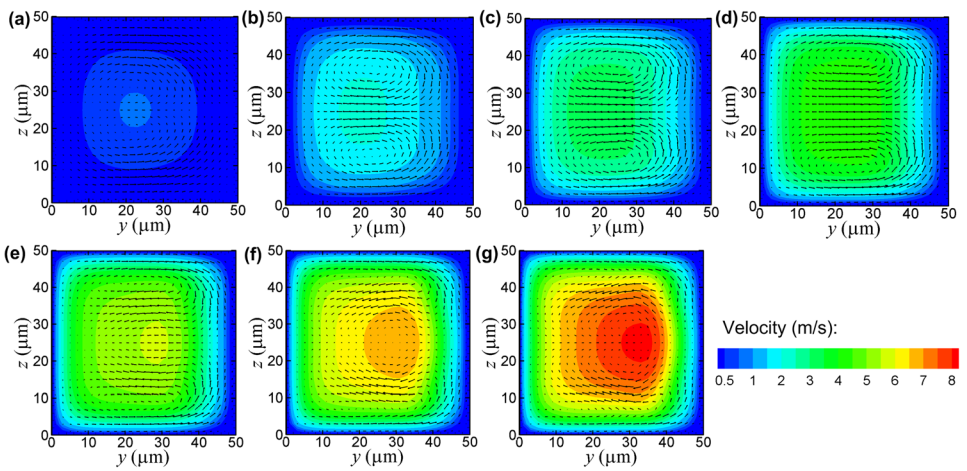

FIG. 5. Total velocity (contour legend) and cross-section velocity distribution (arrows) under various flow rates: (a) 50 μl/min; (b) 150 μl/min; (c) 250 μl/min; (d) 350 μl/min; (e) 450 μl/min; (f) 550 μl/min; and (g) 650 μl/min.

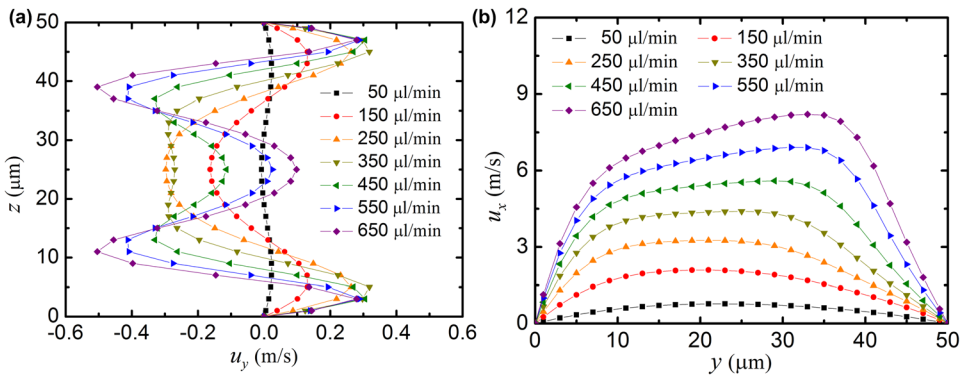

FIG. 6. Dean flow velocity distribution over the cross-section under various flow rates: (a) y-velocity distribution along the vertical center line of the cross-section and (b) x-velocity distribution along the horizontal center line of the cross-section.

particle migration into the vortex, usually $\mathrm{Re} < 100$. Decreasing the cavity width moves the peak velocity towards the channel center slightly and elongates the distance between vortex centers of the Dean flow when the inlet flow rate is 150 μl/min (see Figures S2(a) and S2(b) of the supplementary material[27]). The cavity length has even less influence on the Dean flow (see Figures S2(c) and S2(d) of the supplementary material[27]).

D. Experimental research on flow patterns in rectangular cavity

A prototype polydimethylsiloxane (PDMS) microfluidic device depicted in Figure 7(b) was designed and then fabricated using the maskless lithography technique. The configuration and dimension of this device are the same as those used in the simulation model. In order to visually illustrate the flow patterns in the rectangular cavity, trace particles were artificially added to the test fluid sample. The 2 μm-diameter dyed polystyrene particles solution (B0200, Thermo Fisher Scientific, Inc.) with an initial particle concentration of 1% was diluted with deionized water containing 0.5% (mass ratio) Tween 20 (Sigma-Aldrich). The function of the Tween is to reduce the agglomeration of particles and then further improve the accuracy of the streamline

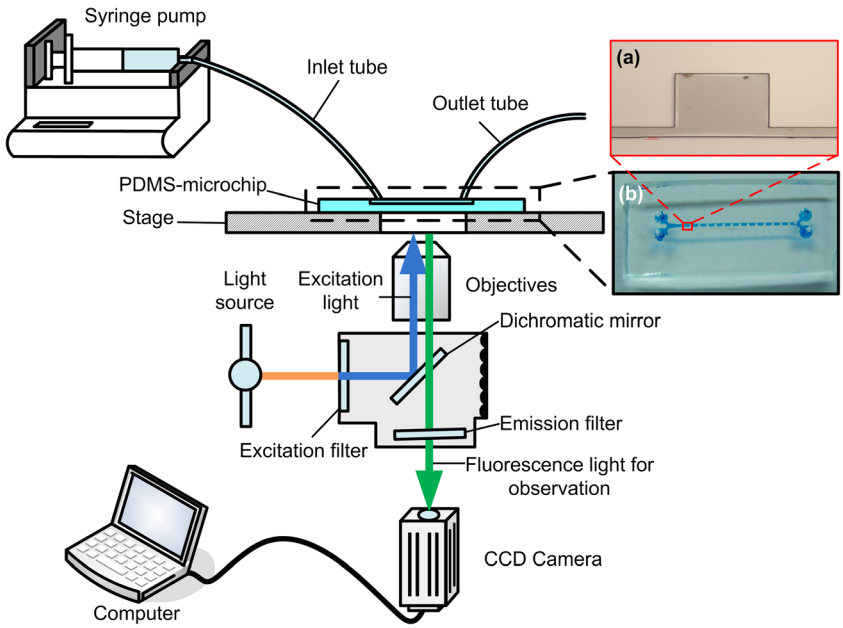

FIG. 7. Schematic diagram of experimental setup. (a) A microscope image of the first rectangular cavity in the microchannel and (b) a photo of the microfluidic device.

tracer. The parameters of the final test solution such as density and viscosity are also identical with those used in the simulation model.

A schematic diagram of the experimental setup is shown in Figure 7. The test solution was pumped into the microchannel via a programmable syringe pump (KDS201, KD Scientific, Inc.) and a short piece of polyetheretherketone (PEEK) tubing (1569, Upchurch Scientific), so that the flow rate can be kept constant during the experiment. The flow pattern in the first cavity of the microchannel was observed and recorded by using a 10× objective lens and a fluorescence mirror unit (U-MWU2) equipped in an inverted fluorescent microscope (IX71, Olympus). The microscope images of the flow pattern were captured by utilizing a 14-bit CCD camera (Exi Blue, Qimaging) with an exposure time of ∼2 s. The walls of the microchannel were located precisely by stacking the fluorescence images with a bright field image which clearly depicted the structure of the microchannel.

The flow rate was set to increase from 50 μl/min to 650 μl/min (with an increment of 100 μl/min) during the experiments. Microscope images of the flow pattern are shown in Figures 8(a)–8(g). Three dimensional surface plot of the grayscale value across the fluorescence images was used to assist in evaluating the plane vortices. The grayscale shades can partly represent the concentration of the particles. From these figures, the whole formation process of a vortex in the cavity can clearly observed. Specifically, the fluorescence particles spread over the cavity as the test solution flows through the microchannel and only two small empty regions appear in the corners (Figure 8(a)) when the flow rate is 50μl/min. With the flow rate increasing to 150 μl/min, fluorescence empty appears near the inlet region of the cavity and continues to grow with flow rates (Figures 8(b) and 8(c)). A vortex can be observed as the flow rate increases to 350 μl/min (Figure 8(d)). And this vortex region occupies the cavity when the flow rate is higher (Figures 8(e)–8(g)). It should be particularly noticed that when the flow rate is higher than 550 μl/min, particle aggregation appears in the vortex center. Furthermore, the vortex leads to a particle-concentration gradient formed. It can be seen that with the increasing inlet flow rate, more particles can be trapped in the vortex region. This finding of the particle aggregation and particle-concentration gradient generated by the vortex can be valuable for the high-efficient mixing and manipulation of micro/nanomaterials.

Comparison results of the vortex centers measured from both the simulation and experiment are shown in Figure 8(h) and the two groups of results have similar trends. In addition, the flow pattern and even the streamlines obtained from the experiment are in good agreement with those of the simulation. The difference between two groups is relatively larger only when

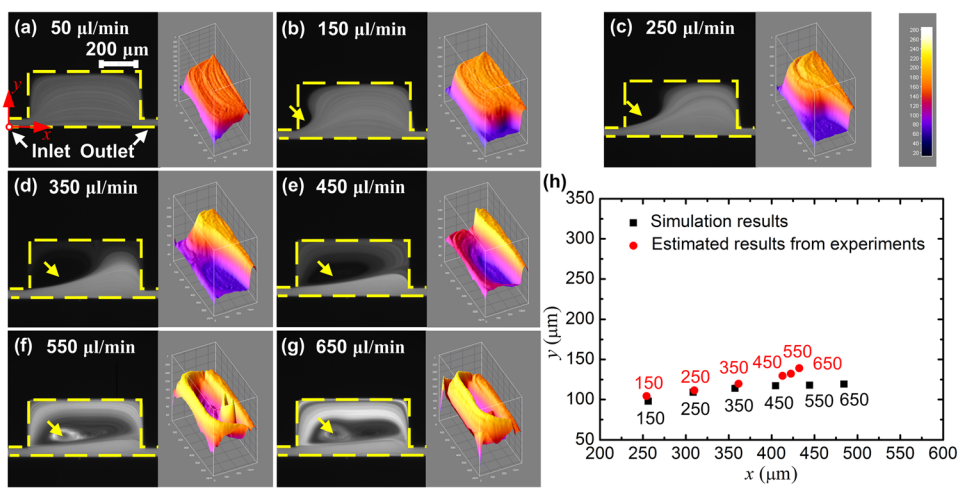

FIG. 8. Microscope images of the flow patterns in the rectangular cavity. (a)–(g) Microscope images of the flow patterns in the rectangular cavity and corresponding 3D surface plot of grey scale under flow rate as 50 μl/min–650 μl/min (yellow arrows point to estimated vortex centers). (h) Comparison diagram of vortex centers from the simulation and experiment, respectively (unit: μl/min).

the inlet flow rate is higher than 550 μl/min, this is because there is a second vortex center generated next to the main one. Pressure boundary condition in the simulation cannot be completely identical to the velocity inlet in the first cavity of the expansion-contraction array, and the simulation results will be more in accord with the other cavities in the whole array. From these results, we can conclude that the LBM can be a powerful approach to predict the flow field in a microchannel.

IV. CONCLUSIONS

This paper applied LBM to a 3D simulation of flow field in an expansion-contraction microchannel. Through these simulations of flow characters in the rectangular cavity under different inlet flow rates, the formation processes of vortex and Dean flow in the microchannel were elucidated systematically. With flow rates ranging from 50 μl/min to 350 μl/min, a vortex was generated near the inlet of the cavity and moved towards the outlet with growing size. The Dean flow also became more obvious as the inlet flow rate increasing. When the flow rate was as high as 450 μl/min, the vortex region fully occupied the cavity and the velocity peak moved from the left region to the right of the outlet cross-section. Cavity dimensions are also investigated here with various widths and lengths under 150 μl/min inlet flow rate. A smaller width is helpful for a larger vortex formation and moves the peak velocity back to the channel center, but cavity length has less influence on the flow feature in this simulation. Then, we performed corresponding experiments to verify the accuracy of the simulation. Research results in this work are of significance for guiding the design of microfluidic systems for particle separation and biological detection.

ACKNOWLEDGMENTS

This research work was supported by the Major Program of the National Natural Science Foundation of China (Grant No. 91023024), the National Basic Research Program of China (Grant No. 2011CB707601), the Specialized Research Fund for the Doctoral Program of Higher Education (Grant No. 20110092110003), Jiangsu Natural Science Foundation (Grant No. BK2011336), and the Jiangsu Industry-University-Research Cooperative Innovation and Prospective Study (Grant No. BY2011135).

[1]J. R. SooHoo, J. K. Herr, J. M. Ramsey, and G. M. Walker, Anal. Chem. **84**, 2195 (2012).
[2]J. H. Kang, S. Krause, H. Tobin, A. Mammoto, M. Kanapathipillai, and D. E. Ingber, Lab Chip **12**, 2175 (2012).
[3]P. S. Dittrich and P. Schwille, Anal. Chem. **75**, 5767 (2003).
[4]P. Garstecki, M. J. Fuerstman, M. A. Fischbach, S. K. Sia, and G. M. Whitesides, Lab Chip **6**, 207 (2006).
[5]J. Zhe, A. Jagtiani, P. Dutta, J. Hu, and J. Carletta, J. Micromech. Microeng. **17**, 304 (2007).
[6]D. C. Duffy, J. C. McDonald, O. J. A. Schueller, and G. M. Whitesides, Anal. Chem. **70**, 4974 (1998).
[7]A. Karimi, S. Yazdi, and A. M. Ardekani, Biomicrofluidics **7**, 021501 (2013).
[8]L. R. Huang, E. C. Cox, R. H. Austin, and J. C. Sturm, Science **304**, 987 (2004).
[9]H. C. Lee, H. H. Hou, R. J. Yang, C. H. Lin, and L. M. Fu, Microfluid. Nanofluid. **11**, 469 (2011).
[10]A. A. S. Bhagat, S. S. Kuntaegowdanahalli, and I. Papautsky, Lab Chip **8**, 1906 (2008).
[11]H. S. Moon, K. Kwon, K. A. Hyun, T. S. Sim, J. C. Park, J. G. Lee, and H. I. Jung, Biomicrofluidics **7**, 014105 (2013).
[12]C. M. Bălan, D. Broboană, and C. Bălan, Microfluid. Nanofluid. **13**, 819 (2012).
[13]C. H. Tsai, H. T. Chen, Y. N. Wang, C. H. Lin, and L. M. Fu, Microfluid. Nanofluid. **3**, 13 (2007).
[14]C. H. Tsai, C. P. Yeh, C. H. Lin, R. J. Yang, and L. M. Fu, Microfluid. Nanofluid. **12**, 213 (2012).
[15]C. H. Tsai, C. H. Lin, L. M. Fu, and H. C. Chen, Biomicrofluidics **6**, 024108 (2012).
[16]Z. T. F. Yu, Y. Lee, M. Wong, and Y. Zohar, J. Microelectromech. Syst. **14**, 1386 (2005).
[17]J. S. Park, S. H. Song, and H. I. Jung, Lab Chip **9**, 939 (2009).
[18]A. J. Mach, J. H. Kim, A. Arshi, S. C. Hur, and D. Di Carlo, Lab Chip **11**, 2827 (2011).
[19]S. C. Hur, A. J. Mach, and D. Di Carlo, Biomicrofluidics **5**, 022206 (2011).
[20]M. G. Lee, S. Choi, H. J. Kim, H. K. Lim, J. H. Kim, N. Huh, and J. K. Park, Appl. Phys. Lett. **98**, 253702 (2011).
[21]M. G. Lee, S. Choi, and J. K. Park, J. Chromatogr., A **1218**, 4138 (2011).
[22]S. Chen and G. D. Doolen, Annu. Rev. Fluid Mech. **30**, 329 (1998).
[23]D. Kandhai, D. Vidal, A. Hoekstra, H. Hoefsloot, P. Iedema, and P. Sloot, Int. J. Numer. Methods Fluids **31**, 1019 (1999).
[24]Y. Qian, D. D'Humières, and P. Lallemand, Europhys. Lett. **17**, 479 (1992).
[25]X. He, Q. Zou, L. S. Luo, and M. Dembo, J. Stat. Phys. **87**, 115 (1997).
[26]Z. Guo, C. Zheng, and B. Shi, Chin. Phys. **11**, 366 (2002).
[27]See supplementary material at http://dx.doi.org/10.1063/1.4812456 for Figures S1 and S2.
[28]R. Du and B. C. Shi, J. Hydrodynamics **22**, 782 (2010).
[29]G. Guj and F. Stella, J. Comput. Phys. **106**, 286 (1993).